# Quartic Dispersion, Strong Singularity, Magnetic Instability, and Unique Thermoelectric Properties in Two-Dimensional Hexagonal Lattices of Group-VA Elements

Hâldun Sevinçli*[iD]

Department of Materials Science and Engineering, Izmir Institute of Technology, 35430 Urla, Izmir Turkey

**S** *Supporting Information*

**ABSTRACT:** The critical points and the corresponding singularities in the density of states of crystals were first classified by Van Hove with respect to their dimensionality and energy-momentum dispersions. Here, different from saddle-point Van Hove singularities, the occurrence of a continuum of critical points, which give rise to strong singularities in two-dimensional elemental hexagonal lattices, is shown using a minimal tight-binding formalism. The model predicts quartic energy-momentum dispersions despite quadratic or linear ones, which is also the origin of the strong singularity. Starting with this model and using first-principles density functional theory calculations, a family of novel two-dimensional materials that actually display such singularities are identified and their extraordinary features are investigated. The strong singularity gives rise to ferromagnetic instability with an inverse-square-root temperature dependence and the quartic dispersion is responsible for a steplike transmission spectrum, which is a characteristic feature of one-dimensional systems. Because of the abrupt change in transmission at the band edge, these materials have temperature-independent thermopower and enhanced thermoelectric efficiencies. Nitrogene has exceptionally high thermoelectric efficiencies at temperatures down to 50 K, which could make low-temperature thermoelectric applications possible.



**KEYWORDS:** *Two-dimensional materials, quartic dispersion, Van Hove singularity, magnetic instability, thermoelectricity*
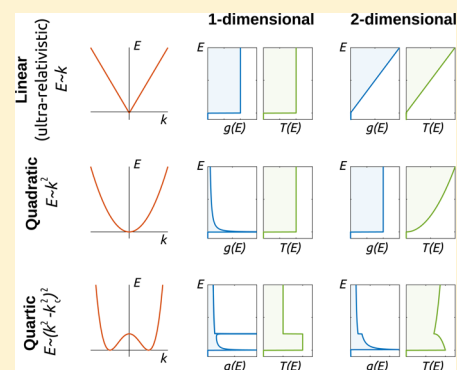
Recent developments in materials research have underlined the unique role of dimensionality in determining the properties of materials. One of the most remarkable examples has been graphene, by which unprecedented properties have been possible due to reduced dimensionality. Among other quantities, electronic density of states (DOS, $g(E)$) has a special role in the physical properties and it is determined by the dimension of the crystals, $d$, and the energy-momentum dispersion relation, $E(\mathbf{k})$. Therefore, discontinuities and singularities in the DOS at the critical points have particular importance. The general case is the occurrence of non-degenerate critical points and their classification is due to Van Hove.[1] Van Hove singularities are responsible for quantum phase transitions, they are related to superconductivity and magnetism, and are crucial in transport phenomena and nanoscale physics and chemistry.[2−6]

In two- and three-dimensional crystals (2D and 3D, respectively), saddle points give rise to weak singularities (logarithmic and square-root, respectively). In 3D, the singularities are observed as discontinuities in $\partial g/\partial E$. On the other hand, in 1D the singularities are strong and are not only due to saddle points but are also due to local minima and maxima. In Figure 1, linear ($E \sim k$), quadratic ($E \sim k^2$), and quartic ($E \sim (k^2 - k_c^2)^2$) energy-momentum dispersions are plotted and their DOS and transmission spectra (TS) are shown for 1D and 2D systems. In 2D systems with linear dispersion, there exists a discontinuity in $\partial g/\partial E$, whereas 1D systems with linear dispersion and 2D systems with quadratic dispersion display discontinuities in $g$ at the band edges. There exist strong inverse-square-root singularities in 1D quadratic and 2D quartic bands. The 2D quartic band displays an additional discontinuity in $g$ due to the local extrema at the zone center. Whereas 1D TS are always stepwise, 2D linear and quadratic dispersions correspond to linear and square-root behavior in TS, respectively. On the other hand, here it is shown that steplike changes in TS, as in 1D, are possible for the 2D quartic case.

Occurence of strong singularities in 2D are linked to a richness of phenomena ranging from superconductivity to spontaneous magnetization and high thermopower.[3−5] For example, a degenerate but isolated singularity was observed in superconducting $YBa_2Cu_4O_8$ and was related to the so-called Van Hove scenario of high-$T_c$ superconductivity.[6] Also gallium and indium monochalcogenide structures were recently reported to display such singularities and were predicted to display multiferroic character, tunable magnetism, and half-metallicity.[3,7]
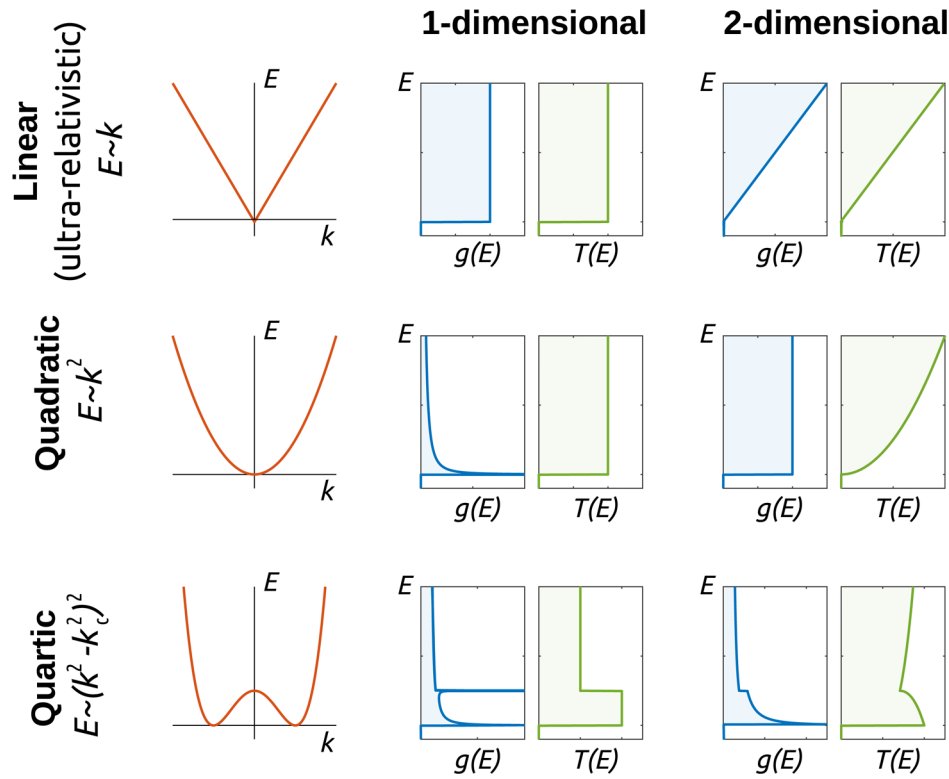
**Figure 1.** Density of states ($g$) and transmission spectrum ($\mathcal{T}$) in one- and two-dimensional crystals for different energy-momentum dispersions. In 1D, there is strong singularity for both quadratic and quartic dispersions. In 2D, strong singularity exists only for the quartic dispersion. In 1D, the transmission spectra are stepwise, whereas in 2D there is a stepwise change only for the quartic dispersion, which is at the critical point.

Here, we report the occurrence of quartic dispersions and associated nonisolated degenerate singularities (cf. Figure 1) in novel 2D crystals of group-VA elements and show that they have unique electronic and magnetic properties. We also investigate the electronic and thermal transport properties of these materials and find that spin susceptibility scales with $T^{-1/2}$. The 2D quartic dispersion is not only responsible for inverse-square-root singularity in the DOS but it also gives rise to a step-like electronic transmission spectrum. Stepwise changes in electronic transmission is a general case for 1D systems independent of the type of dispersion and they are known to give rise to novel features like enhanced thermoelectric efficiency. Here, it is shown that steplike transmission in 2D gives rise to not only enhancement of the efficiency but also to peculiar features like temperature-independent thermopower and superior ZT values at low temperatures.

**Electronic Structure.** We start with investigating the single-layer hexagonal lattice (see Figure 2a), using an empirical tight binding (TB) Hamiltonian with second nearest neighbor interactions

$$H = -t_1 \sum_{\langle i,j \rangle} (c_i^\dagger c_j + h.c.) - t_2 \sum_{\langle\langle i,j \rangle\rangle} (c_i^\dagger c_j + h.c.) \tag{1}$$

where $c_i$ ($c_i^\dagger$) annihilates (creates) an electron at the $i$th site, the first summation runs over the first nearest neighbors, and the second summation runs over the next-nearest neighbors. This Hamiltonian has a quite general form and the corresponding bands have energies $E_\pm(\mathbf{k}) = \pm t_1 \sqrt{(3 + f(\mathbf{k}))} - t_2 f(\mathbf{k})$ with $f(\mathbf{k}) = 2\cos(\sqrt{3}k_y a) + 4\cos(\sqrt{3}k_y a/2)\cos(3k_x a/2)$, $a$ being the lattice constant, and $\mathbf{k}$ is a vector in the reciprocal space (Figure 2b). For a suitable choice of $t_1$ and $t_2$, the energy bands

$E_\pm$ reproduce the first valence and conduction bands of graphene.[8,9] Replacing carbon with atoms of graphene with group-VA elements, one more band is filled and the above Hamiltonian gives two of their valence band dispersions with $E_+$ forming the top valence band and it is our main focus.

First, we investigate the critical points and the DOS of $\varepsilon = E_+/t_1$. Around the center of the reciprocal space ($\Gamma$-point), one can expand $\varepsilon$ to obtain the isotropic expression, $\varepsilon \simeq (3 - 6\xi) - (ka)^2(3 - 18\xi)/4 + (ka)^4(3 - 54\xi)/64$, where $\xi = t_2/t_1$. For the special case of $\xi = 1/6$, there exists a degenerate isolated critical point at $\Gamma$ with $\varepsilon \propto k^4$, which generates a strong (inverse-square-root) singularity. Apart from this special case, $\varepsilon$ has critical points for $k > 0$ provided that $\xi > 1/6$. Eventually, the determinant of the Hessian, $|\partial^2\varepsilon/\partial k_\alpha \partial k_\beta|$, vanishes not only for a number of isolated $\mathbf{k}$-points but the degenerate critical points form a closed curve around $\Gamma$. The occurrence of closed curves of degenerate critical points is not only for some exceptional sets of parameters but of a more general nature.

It is convenient to identify the nonisolated degenerate critical points in cylindrical coordinates, $(k,\theta)$. Following Van Hove, one expands $\varepsilon$ around the critical points; because $\partial\varepsilon/\partial k$ vanishes when $f = \xi^{-2}/4 - 3$, $\varepsilon$ has a quartic dependence on $k$ (see Figure 2) and the maxima forms an approximate circle with radius $k_c = 2/3a \, \text{Arccos}(\xi^{-2}/16 - 5/4)$. As a result, the energy-momentum relation around $k_c$ is obtained as

$$\varepsilon = \varepsilon_v - \alpha(k^2 - k_c^2)^2 \tag{2}$$

with $\varepsilon_v = \xi^{-1}/4 + 3\xi$ and $\alpha = k_c^{-4}(\xi^{-1}/4 - 3 + 9\xi)$, which is in very good agreement with the full solution of eq 1, around the $\Gamma$-point. (see Figure 2c) Consequently, the density of states can be written as
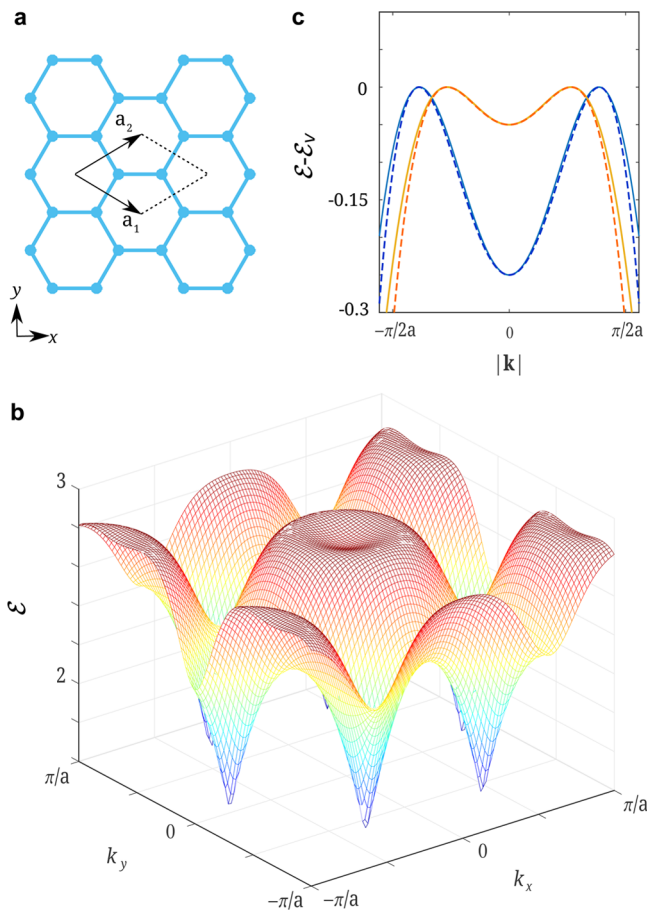
a



c



b



**Figure 2.** Hexagonal lattice and energy dispersions. (a) The unit cell is depicted with dotted lines with $\mathbf{a}_1$ and $\mathbf{a}_2$ being the lattice vectors. (b) Tight binding energy dispersion of $\varepsilon$ is plotted in units of $t_1$ for $-\pi/a \leq k_x, k_y \leq \pi/a$ and $\xi = 0.2$ with the Mexican hat shape centered at the origin of the Brillouin zone. (c) The continuum equation $\varepsilon - \varepsilon_v = -\alpha(k^2 - k_c^2)^2$ (dashed curves) is compared against the tight-binding model (solid curves) for $\xi = 0.2$ and $\xi = 0.25$ (orange and blue, respectively).

$$g(\varepsilon) = \frac{\pi}{2}\sqrt{\frac{\alpha}{\varepsilon_v - \varepsilon}}\left[1 + \theta(\varepsilon - \varepsilon_v + \alpha k_c^4)\right] \tag{3}$$

for $\varepsilon < \varepsilon_v$ and zero otherwise. $g(\varepsilon)$ has an inverse-square-root singularity at the band edge, just like one-dimensional crystals with quadratic dispersion (see Figure 1). Because the band maxima forms a closed curve around the zone center, the value of $g(\varepsilon)$ could be expected to depend on the length of the curve, therefore on $k_c$. Besides, $g$ is proportional to $\sqrt{\alpha}$ and independent of $k_c$, a consequence of system's two-dimensional nature. These features are the characteristics of quartic dispersion in 2D.

Graphene-like $sp^2$ hybridized systems with two additional electrons per unit cell, namely hexagonal lattices of group-VA elements, are expected to display strong singularities, provided that $\xi$ lies within the required range. Recently, monolayers of nitrogen, phosphorus, arsenide, antimony, and bismuth were reported to have stable hexagonal structures[10−17] and they are referred to as nitrogene, phosphorene, arsenene, antimonene, and bismuthene. Puckered geometries of these elements were also reported but they are not the subject of current study. Unlike graphene, the hexagonal structures of group-VA elements are nonplanar. (Figure 3a) Atoms of different

sublattices have different heights to form a buckled structure and vibrational analyses predict them as stable (see Supporting Information).

We performed first-principles density functional theory (DFT)[18,19] calculations to investigate their electronic, vibrational, and transport properties (see Methods section for details). Their electronic structures display the expected quartic dispersions and corresponding strong singularities. For phosphorene and nitrogene, the singularities are at valence band edges, whereas for arsenene, antimonene, and bismuthene other bands form the valence band maximum and the singularities are 0.34, 0.46, and 0.74 eV below the band edges, respectively (see Figure 3). The presence of other bands at the same energy window with the singularities gives rise to complicated features in the DOS of these structures. Still, the singularities are clearly distinguished. Electronic band structure of bismuthene has an avoided band crossing close to the critical point between $\Gamma$ and K (Figure 3g), which indicates a non-negligible mixing of bands. Therefore, the quartic dispersion and the singularity are altered significantly. A comparison of the valence band dispersion from DFT calculations and the quartic formula for nitrogene is shown in Figure 4a, and the singular behavior of the DOS around $E_v$ is shown in Figure 4b. $\alpha$ and $k_c$ of group-VA elemental lattices are given in Table 1. The TB approximation and the quartic formula reproduce these bands successfully around the critical points.

**Magnetic Instability.** Van Hove singularities are known to give rise to quantum phase transitions.[2] In 2D materials, the presence of logarithmic singularities in the DOS were shown to give rise to magnetic phase transitions, where the spin susceptibility depends on the logarithm of inverse temperature.[20] Therefore, the occurrence of strong singularity deserves an investigation of the magnetic instabilities. Using the quartic dispersion and the corresponding DOS, one can show that the spin susceptibility can be approximated as

$$\chi(T) \approx \frac{\gamma\pi}{4}\sqrt{\frac{\alpha}{k_B T}} \tag{4}$$

with $\gamma = 1.91$ (see Methods section for further details). Similar to the DOS, $\chi$ is independent of $k_c$ but scales with $\sqrt{\alpha}$. Here, the chemical potential is assumed to be at the valence band maximum (VBM), which enables a magnetic state. Ferromagnetic instabilities give rise to a wide-range of phases. In $\alpha$-SnO, for example, Mexican hatlike dispersion was shown to give rise to ferroplastic, paraelastic, and multiferroic phases depending on the number of layers and doping density.[3] The ferromagnetic instability indicates the possibility of magnetic phase transitions upon p-type doping of the material.

**Transmission Spectrum.** In addition to the strong singularity in the DOS, quartic dispersion has crucial consequences in the TS as well. Because the number of conduction channels is proportional to the radii of the iso-energy curves, ballistic TS becomes $\mathcal{T}(\varepsilon) = \theta(\varepsilon_v - \varepsilon)(k_1 + k_2)a/\pi$, where $k_{1,2}$ are the solutions of eq 2. More explicitly, one has

$$\mathcal{T}(\varepsilon) = \frac{k_c a}{\pi}\left[\left(1 + \sqrt{\frac{\varepsilon - \varepsilon_v}{\alpha k_c^4}}\right)^{1/2} + \left(1 - \sqrt{\frac{\varepsilon - \varepsilon_v}{\alpha k_c^4}}\right)^{1/2}\right] \tag{5}$$

for $\varepsilon < \varepsilon_v$ and zero otherwise. In the lowest order expansion, $k_1 + k_2 = 2k_c$ and $\mathcal{T} = \theta(\varepsilon_v - \varepsilon)2k_c a/\pi$. Contrary to the DOS
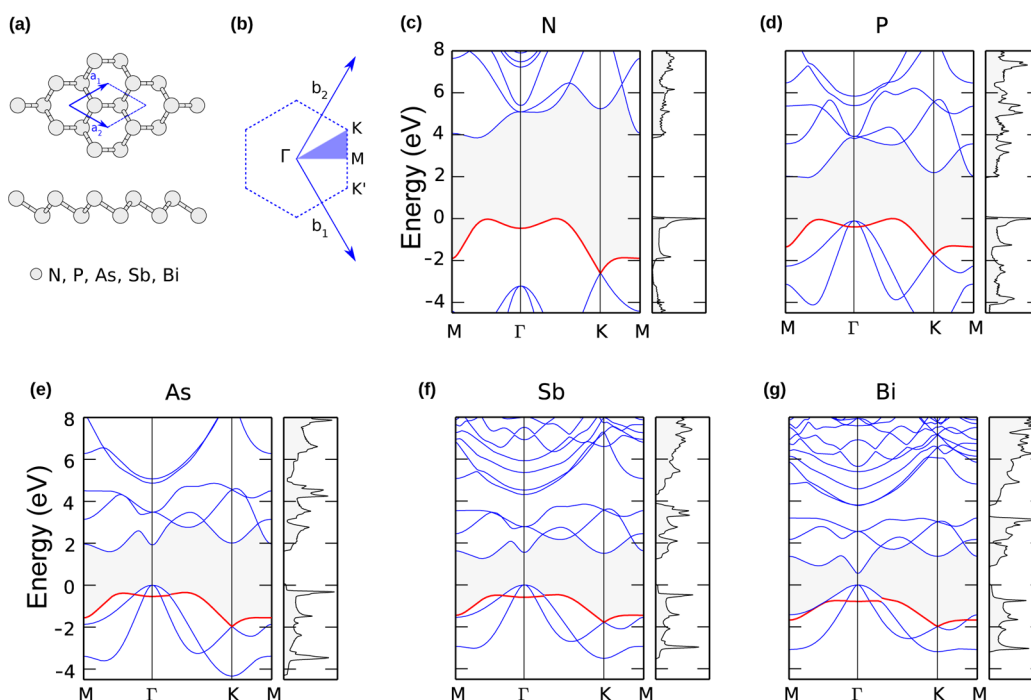
**Figure 3.** Crystal structure and electronic energy bands of two-dimensional hexagonal lattices of group-VA elements. (a) Crystal lattice structure, (b) the reciprocal lattice and the high symmetry points of elemental hexagonal lattices, and the electronic energy band diagrams of 2D hexagonal N, P, As, Sb, and Bi (c−g). The valence band maximum is set to the zero of the energy axis and the energy band gaps are shaded. The bands with quartic dispersion around Γ-point are plotted in red.

(cf. eq 3) TS is determined mainly by $k_c$, and $\alpha$ appears only after higher order expansions. More interestingly, the lowest order approximation yields a step function in the TS. This behavior, like the presence of strong singularity in the DOS, is a characteristic feature of one-dimensional systems. An outcome of such abrupt changes in the TS is the enhancement of thermoelectric efficiency, as it will be discussed below.[21,22] Comparison of the TS obtained from DFT to that from eq 2 yields excellent agreement (Figure 4c). Step-function is a good approximation for TS, especially around the band edge.

**Thermoelectric Transport.** Thermoelectric coefficients are determined by using the integrals

$$L_n(\mu, T) = -\frac{2}{h}\int dE \frac{\partial f_{FD}}{\partial E}(E - \mu)^n \mathcal{T}(E) \qquad (6)$$

where $\mu$ is the chemical potential, $T$ is temperature, $h$ is Planck's constant, and $f_{FD}$ is Fermi−Dirac distribution function. Using $L_n$, the electrical conductance, Seebeck coefficient, and the electrical part of thermal conductance are defined as $G = e^2 L_o$, $S = (L_1/L_o)/eT$ and $\kappa_{el} = (L_2 - L_1^2/L_o)/T$, respectively, with $e$ being the electron charge.[23,24] Finally, the power factor and the thermoelectric figure of merit are obtained as $P = S^2 G$ and $ZT = S^2 GT/(\kappa_{el} + \kappa_{ph})$, $\kappa_{ph}$ being the phononic thermal conductance[25] (see eq S1 in Supporting Information).

In the step-function approximation of the TS, $L_n$ can be obtained analytically for $\mu = \varepsilon_v$ hence the values of $G$ and $P$ are proportional to the step height while $S$ is independent of it. Moreover, $S$ is independent of the temperature and it is equal to 0.119 mV/K ($S = 2k_B/|e|\ln 2$), a universal value for step-function transmission independent of the material (i.e., the height of the step) and temperature. Temperature-independent thermopower was previously reported in cuprate super-conductors and it was related to the presence of Van Hove

singularity.[26] Here, it is due to the steplike TS, which is a manifestation of the quartic dispersion in 2D.

In Figure 4d,e, the Seebeck coefficient and power factor of nitrogene as obtained by using DFT are plotted as functions of the chemical potential at different temperatures. $S$ values increase inside the band with temperature, whereas the reverse is true in the band gap. $S \approx 0.11$ mV/K at $\mu = E_v$ as it was also predicted from analytical calculations. It is noted that very high $S$ values can be obtained inside the band gap, the maximum being close to the middle of the gap. These are not the true indications of large thermoelectric efficiency, but thermoelectric power factor $P = S^2 G$ and figure of merit $ZT = PT/\kappa$ are the reliable quantities. Unlike $S$, $P$ has local maxima close to the band edge and decays inside the gap because conductance decreases exponentially inside the band gap (Figure 4e).

In Figure 5, thermoelectric properties of group-VA hexagonal lattices are plotted as functions of the chemical potential at room temperature around the valence band edge. Abrupt changes in the transmission values occur at band maxima for nitrogene and phosphorene, while similar phenomena occur inside the band for the rest of the structures. (Figure 5a) Ballistic electrical conductance values are similar to the transmission spectra with smoothening due to temperature. All structures have high $S$ around the band maxima. (Figure 5b) For arsenene, antimonene, and bismuthene there are local maxima coinciding with the steplike change in the TS in (Figure 5a). The advantage of steplike transmission is evident in the power factor, where nitrogene and phosphorene have largest values at $\mu = E_v$ (Figure 5c). $P$ of arsenene, antimonene, and bismuthene have peaks inside the band at the same energies with those of $S$ but with smaller peak values. We note that these structures have maxima at the VBM as well due to onset of the quadratic band, and all three structures have the same peak values in parallel with their TS having very similar
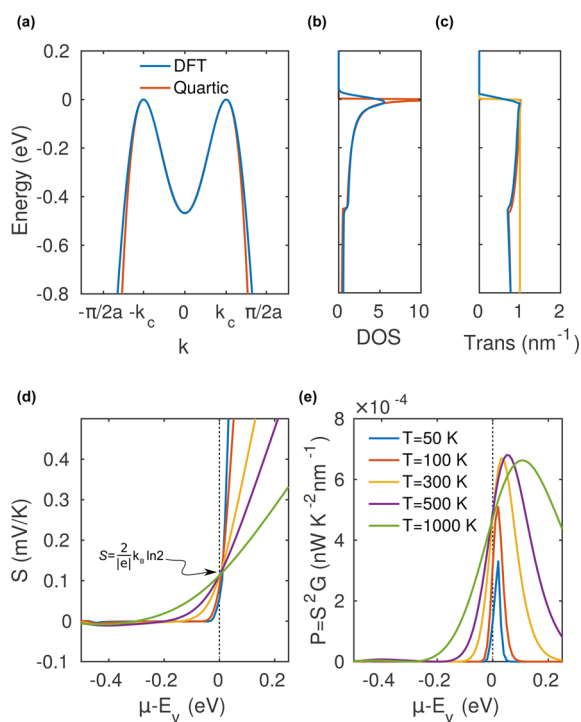
**Figure 4.** Quartic dispersion, strong singularity, peculiar transmission, and thermoelectric coefficients of nitrogene. Density functional theory results are compared against those from the quartic dispersion formula (a–c), where zero of the energy is set to the valence band edge. (a) The valence band dispersion of hexagonal nitrogene from DFT calculations and the quartic dispersion relation (cf. eq 2). (b) The corresponding DOS is shown where the softening of the singularity in the DFT result is within the accuracy of the smearing effect in the numerical results. (c) Transmission spectra obtained from DFT calculations are compared against eq 5. The step function from the lowest order approximation is also given for comparison. (d) Thermopower ($S$) is plotted for various temperatures as a function of the chemical potential measured from the VBM, $\mu - E_v$. $S = 2k_B/|e| \ln 2$ at all temperatures of $\mu = E_v$. (e) Power factor for the same temperatures as a function of $\mu - E_v$.

**Table 1. Parameters for the Quartic Dispersion Formula**[a]

|  | N | P | As | Sb | Bi |
|---|---|---|---|---|---|
| $\alpha$ (eV Å$^{-4}$) | 1.155 | 2.887 | 3.914 | 5.518 | 8.983 |
| $k_c$ (Å$^{-1}$) | 0.798 | 0.613 | 0.474 | 0.396 | 0.258 |

[a]$k_c$ is the norm of the the critical wave vectors at which the energy has degeneracy on a closed curve around the center of the Brillouin zone, and $\alpha$ is the prefactor (see eq 2).

values around VBM. Having larger $\mathcal{T}$, $\kappa_{el}$ of N and P are larger at the VBM (Figure 2d). Being the lightest atoms in the group, N and P have the largest phononic thermal conductances and Bi has the lowest with their values being 1.35, 0.43, 0.25, 0.11, and 0.09 nW K$^{-1}$ nm$^{-1}$ from the lightest to the heaviest atomic species (see Supporting Information). As a result, room temperature ZT values of N, P, and Sb are close to 0.15; for As and Bi it is 0.075 and 0.22, respectively (Figure 5e). A cautionary note is in order here. Because the transmission values are normalized with width, $G$, $P$, and $\kappa$ are width normalized values, whereas in $S$ and ZT there is no width dependence. Also, thermal conductance ($\kappa$) is given in units nW K$^{-1}$ nm$^{-1}$ and should be distinguished from the generally used unit of thermal conductivity, W m$^{-1}$ K$^{-1}$.
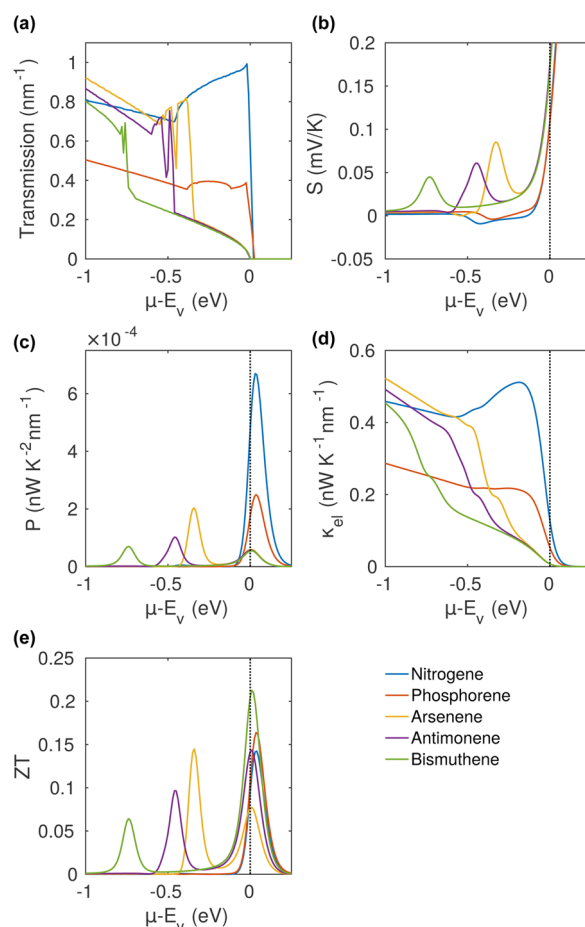


**Figure 5.** Thermoelectric properties at room temerature. (a) Transmission spectra as obtained from DFT simulations. Nitrogene and phosphorene have abrupt step-like changes in transmission due to quartic dispersion at $\mu = E_v$. For arsenene, antimonene, and bismuthene, the onset of quartic dispersion and therefore the steplike changes are at lower energies. However, their transmission spectra are almost the same below $E_v$ until the step. (b) The Seebeck coefficients of As, Sb, and Bi have peaks at the quartic band edges. For N and P, the maxima are inside the band gap and $S \simeq 0.11$ mV/K, as predicted from the analytical calculations. (c) The power factor of N is the largest at the valence band edge. (d) Electrical part of thermal conductance, $\kappa_{el}$ follows the same trend at $\mu = E_v$. Hence the ZT values of N, P, and Sb are close while Bi has the largest value at the band edge and As has the lowest. Change of ordering between $P$ and ZT are mainly because of the phononic thermal transport.

In Figure 6a, phonon thermal conductances ($\kappa_{ph}$) are plotted as functions of temperature, where the influence of atomic mass on vibrational thermal transport is the dominant feature (see Supporting Information for details). Because the vibrational frequencies are inversely proportional with the square roots of the atomic masses, the lightest species, nitrogene, has the highest $\kappa_{ph}$ values (close to 1.5 nW K$^{-1}$ nm$^{-1}$ at 300 K), whereas the heaviest, bismuthene, has the lowest (less than 0.1 nW K$^{-1}$ nm$^{-1}$ at 300 K); the others have intermediate values. The effect of $\kappa_{ph}$ on ZT is significant. The maximum ZT values at different temperatures is plotted in Figure 6b. At high temperatures, the lowest to highest ZT$_{max}$ ordering is the same with the ordering of atomic masses. On the other hand, at room temperature they all have similar ZT$_{max}$ values. One should note that the maximum ZT values for Sb and Bi are achieved around
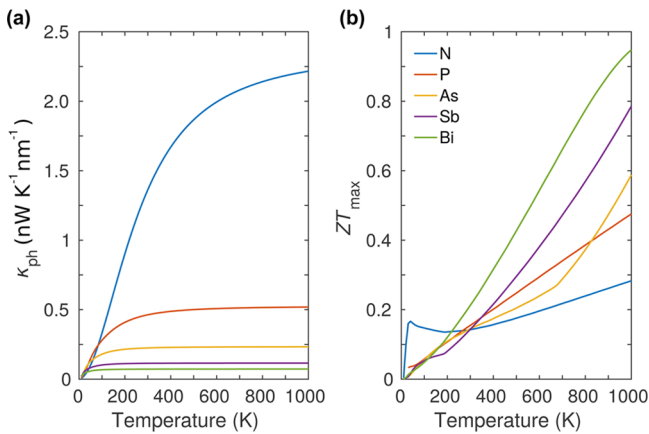
**Figure 6.** Lattice thermal conductance and $ZT_{max}$. $\kappa_{ph}$ and the maximum *of ZT* values for $\mu$ around $E_v$ are plotted as functions of temperature. N and P have considerably higher $\kappa_{ph}$ at the entire range except low $T$. Consequently, they have lower $ZT_{max}$. N has large $ZT_{max}$ below 200 K.

$\mu = E_v$ in place of their quartic band edges, which is primarily due to the high $\kappa_{el}$ at these energies.

More interestingly, when $T < 200$ K, nitrogene supplies significantly higher merit. This is both due to its superior power factor (cf. Figure 5c) and $\kappa_{ph}$ being comparable to the others at these temperatures. A comparison of the ratio $\kappa_{el}/\kappa_{ph}$ at $\mu = E_v$ reveals that it is monotonously increasing with temperature for As, Sb, and Bi but for N and P it has a local maxima at around 50 K and a local minima at intermediate temperatures (300 and 150 K, respectively) (see Supporting Information). At high temperatures, the ratio is significantly higher for As, Sb, and Bi. Even though N has high $\kappa_{ph}$, its $\kappa_{el}$ is substantially higher than others, which gives rise to superior ZT at low $T$.

**Conclusion.** Hexagonal symmetry in monolayers of group-VA elements gives rise to quartic energy-momentum dispersion. Quartic dispersion in 2D is responsible for the strong singularity in the DOS and steplike TS, resembling quasi-1D materials. The inverse-square-root singularity results in ferromagnetic instability with an inverse-square-root dependence on temperature. The step-like TS enables a temperature-independent thermopower and enhanced thermoelectric power factors. When combined with low phononic thermal conductances at low temperature, it becomes possible to have unprecedented thermoelectric efficiencies at low temperatures.

**Methods.** *Density Functional Theory Calculations.* We use plane-wave basis sets[27,28] and the projector augmented wave pseudopotentials[29,30] together with the generalized gradient approximation[31] of the exchange-correlation potential. Structural optimizations are carried out within a force tolerance of $10^{-4}$ eV Å$^{-1}$ per atom using the conjugate gradient algorithm, while the convergence criteria for self-consistent energy calculations are set to $10^{-7}$ eV. Monkhorst−Pack scheme[32] is employed for the sampling of the Brillouin zone with a minimum of $10 \times 10 \times 1$ grid in structural optimizations. In DOS and TS , a fine sampling of $600 \times 600 \times 1$ is used. The atomic force constants are obtained using density functional perturbation theory,[33] from which the vibrational properties are determined.[34]

*Spin Susceptibility Calculation.* Bare spin susceptibility is defined as

$$\chi(T) = -\int \frac{d^2k}{(2\pi)^2} \frac{\partial f_{FD}(\mu, E(k), T)}{\partial E(k)} \tag{7}$$

where $f_{FD}$ is Fermi−Dirac distribution function and the integration is to be performed over the Brillouin zone. Starting with eqs 3 and 7, using $\partial f_{FD}/\partial E = -\cosh^{-2}((E - \mu)/2k_BT)/4k_BT$, and letting $\mu = 0$ one can write

$$\chi(T) = \frac{\pi}{4}\sqrt{\frac{\alpha}{T}} \int_0^\infty dx\, x^{-1/2} \cosh^{-2} x \tag{8}$$

Because the major contribution is from states close to the singularity, one can expand $\cosh(x)$ around zero up to fourth order and perform the integration numerically to get

$$\chi(T) \approx \frac{\gamma\pi}{4}\sqrt{\frac{\alpha}{k_BT}} \tag{9}$$

with $\gamma = 1.91$.

## ASSOCIATED CONTENT

**Ⓢ Supporting Information**

The Supporting Information is available free of charge on the ACS Publications website at DOI: 10.1021/acs.nanolett.7b00366.

Phonon dispersions and transmission spectra; electronic and phononic contributions to thermal conduction (PDF)

## AUTHOR INFORMATION

**Corresponding Author**
*E-mail: haldunsevincli@iyte.edu.tr.

**ORCID** Ⓘ
Hâldun Sevinçli: 0000-0002-1896-2588

**Notes**
The author declares no competing financial interest.

## ACKNOWLEDGMENTS

## REFERENCES

(1) Van Hove, L. *Phys. Rev.* **1953**, *89*, 1189.
(2) Lifshitz, I. M. *Sov. Phys. JETP* **1960**.
(3) Seixas, L.; Rodin, A. S.; Carvalho, A.; Castro Neto, A. H. *Phys. Rev. Lett.* **2016**, *116*, 206803.
(4) Stauber, T.; Peres, N. M. R.; Guinea, F.; Castro Neto, A. H. *Phys. Rev. B: Condens. Matter Mater. Phys.* **2007**, *75*, 115425.
(5) Newns, D. M.; Tsuei, C. C.; Huebener, R. P.; van Bentum, P. J. M.; Pattnaik, P. C.; Chi, C. C. *Phys. Rev. Lett.* **1994**, *73*, 1695−1698.
(6) Gofron, K.; Campuzano, J. C.; Abrikosov, A. A.; Lindroos, M.; Bansil, A.; Ding, H.; Koelling, D.; Dabrowski, B. *Phys. Rev. Lett.* **1994**, *73*, 3302−3305.
(7) Cao, T.; Li, Z.; Louie, S. G. *Phys. Rev. Lett.* **2015**, *114*, 236602.
(8) Wallace, P. R. *Phys. Rev.* **1947**, *71*, 622−634.
(9) Castro Neto, A. C.; Guinea, F.; Peres, N. M.; Novoselov, K. S.; Geim, A. K. *Rev. Mod. Phys.* **2009**, *81*, 109.
(10) Özçelik, V. O.; Aktürk, O. U.; Durgun, E.; Ciraci, S. *Phys. Rev. B: Condens. Matter Mater. Phys.* **2015**, *92*, 165408.

(11) Zhu, Z.; Tománek, D. *Phys. Rev. Lett.* **2014**, *112*, 176802.

(12) Kamal, C.; Ezawa, M. *Phys. Rev. B: Condens. Matter Mater. Phys.* **2015**, *91*, 085423.

(13) Aktürk, O. U.; Özçelik, V. O.; Ciraci, S. *Phys. Rev. B: Condens. Matter Mater. Phys.* **2015**, *91*, 085423.

(14) Ji, J.; Song, X.; Liu, J.; Yan, Z.; Huo, C.; Zhang, S.; Su, M.; Liao, L.; Wang, W.; Ni, Z.; Hao, Y.; Zeng, H. *Nat. Commun.* **2016**, *7*, 13352.

(15) Zhang, S.; Yan, Z.; Li, Y.; Chen, Z.; Zeng, H. *Angew. Chem., Int. Ed.* **2015**, *54*, 3112−3115.

(16) Zhang, S.; Xie, M.; Li, F.; Yan, Z.; Li, Y.; Kan, E.; Liu, W.; Chen, Z.; Zeng, H. *Angew. Chem.* **2016**, *128*, 1698−1701.

(17) Aktürk, E.; Aktürk, O. U.; Ciraci, S. *Phys. Rev. B: Condens. Matter Mater. Phys.* **2016**, *94*, 014115.

(18) Hohenberg, P.; Kohn, W. *Phys. Rev.* **1964**, *136*, B864−B871.

(19) Kohn, W.; Sham, L. J. *Phys. Rev.* **1965**, *140*, A1133−A1138.

(20) Ziletti, A.; Huang, S. M.; Coker, D. F.; Lin, H. *Phys. Rev. B: Condens. Matter Mater. Phys.* **2015**, *92*, 085423.

(21) Mahan, G. D.; Sofo, J. O. *Proc. Natl. Acad. Sci. U. S. A.* **1996**, *93*, 7436−7439.

(22) Hicks, L. D.; Dresselhaus, M. S. *Phys. Rev. B: Condens. Matter Mater. Phys.* **1993**, *47*, 16631−16634.

(23) Ashcroft, N. W.; Mermin, N. D. *Solid state physics*; Saunders College, 1976.

(24) Esfarjani, K.; Zebarjadi, M.; Kawazoe, Y. *Phys. Rev. B: Condens. Matter Mater. Phys.* **2006**, *73*, 085406.

(25) Rego, L. G. C.; Kirczenow, G. *Phys. Rev. Lett.* **1998**, *81*, 232−235.

(26) Newns, D. M.; Tsuei, C. C.; Huebener, R. P.; van Bentum, P. J. M.; Pattnaik, P. C.; Chi, C. C. *Phys. Rev. Lett.* **1994**, *73*, 1695−1698.

(27) Kresse, G.; Hafner, J. *Phys. Rev. B: Condens. Matter Mater. Phys.* **1993**, *47*, 558−561.

(28) Kresse, G.; Furthmüller, J. *Phys. Rev. B: Condens. Matter Mater. Phys.* **1996**, *54*, 11169−11186.

(29) Blöchl, P. E. *Phys. Rev. B: Condens. Matter Mater. Phys.* **1994**, *50*, 17953−17979.

(30) Kresse, G.; Joubert, D. *Phys. Rev. B: Condens. Matter Mater. Phys.* **1999**, *59*, 1758−1775.

(31) Perdew, J. P.; Burke, K.; Ernzerhof, M. *Phys. Rev. Lett.* **1996**, *77*, 3865−3868.

(32) Monkhorst, H. J.; Pack, J. D. *Phys. Rev. B* **1976**, *13*, 5188−5192.

(33) Baroni, S.; de Gironcoli, S.; Dal Corso, A.; Giannozzi, P. *Rev. Mod. Phys.* **2001**, *73*, 515−562.

(34) Togo, A.; Tanaka, I. *Scr. Mater.* **2015**, *108*, 1−5.

## ■ NOTE ADDED AFTER ASAP PUBLICATION

This paper was published on the Web on March 27, 2017. Changes were made to equations 8 and 9, and the corrected version was reposted on March 28, 2017.